ACCSCIENCE PUBLISHING

Design+

ARTICLE

Preliminary configuration and integrated examination of a glider in terms of radar cross-section and remote-sensing characteristics

Zeyang Zhou* and **Jun Huang**

Department of Aircraft Design, School of Aeronautic Science and Engineering, Beihang University, Beijing, China

Abstract

With advances in aircraft design and the application of new energy batteries, gliders with long endurance and good concealment may adversely affect regional safety and low-altitude activities. To study the radar cross-section (RCS) and remote sensing features of the glider, an integrated examination based on electromagnetic scattering assessment and remote sensing imaging is presented. The glider model was preliminarily designed, and the relevant RCS and remote-sensing grayscale were analyzed. The results showed that under the given conditions, the glider's peak RCS reached 25.3957 dBm^2, with the fuselage providing the main scattering contribution. The top surface of the fuselage also appeared light gray in remote-sensing images. The average RCS index of the glider increased by 0.7849 dBm^2 with the increase of the elevation angle within the given range. The wedge-shaped fuselage top created a contrast between light gray and gray on the surfaces on both sides of the body's symmetrical plane in the remote-sensing grayscale image. The grayscale features of the wings, wingtips, fuselage, and tail of the glider can be distinguished, and the orientation of the nose can be determined. In the grayscale image of the glider formation, the visualization of the rear fuselage beam was weakened, and the backward diffusion queue might appear visually complex, while it followed a mathematically predictable sinusoidal pattern. The established approach is effective for analyzing the RCS and remote-sensing characteristics of the glider.

Keywords: Gliding aircraft; Comprehensive analysis; Electromagnetic scattering; Formation flying; Remote-sensing observation

***Corresponding author:**
Zeyang Zhou
(zeyangzhou@buaa.edu.cn)

Citation: Zhou Z, Huang J. Preliminary configuration and integrated examination of a glider in terms of radar cross-section and remote-sensing characteristics. *Design+*. 2026;3(1):026010001. doi: 10.36922/DP026010001

Received: January 4, 2026

Revised: February 25, 2026

Accepted: February 28, 2026

Published online: March 26, 2026

1. Introduction

Gliders can be towed by ground vehicles or launched by airplanes for takeoff, where the high-aspect-ratio wing layout, coupled with a novel energy configuration, can significantly increase their loiter time for optical imaging and radar/infrared remote sensing.[1-3] The formation of multiple gliders may pose adverse effects on low-altitude safety and regional privacy; thus, research on their remote sensing and radar cross-section (RCS) deserves attention.

A micro glider fabricated using a printed circuit board can be launched from a high-altitude super-pressure balloon and glide to the target location to collect data.[4] In high-

latitude regions, covering both the vertical tail and the wings with solar panels can effectively improve the cruise performance of aircraft.[5] 3D printing technology can be utilized to manufacture fuselage and wing components for customization.[6] The aeroelasticity of the high-aspect-ratio wings of solar-powered aircraft has been analyzed previously.[7] The structural materials, photovoltaic system, and battery system of solar-powered aircraft have also been introduced.[8] The concept of designing a flight trajectory for solar-powered aircraft based on gravitational energy storage is feasible.[9] The technical condition data of the glider's fuselage design have been analyzed using bionic logic.[10] This powered glider, equipped with a battery or solar energy configuration, can take off on its own[11-14], with the power device turned on or off as needed. Some gliders feature T-shaped or inclined tailwings at the rear of their fuselage.

High-resolution optical remote-sensing equipment can monitor the ground or low-altitude vehicles during the day, while radar/infrared remote sensing can image aircraft and gliders at night.[15] Artificial magnetic conductors have been used to design surfaces for ultra-wideband RCS reduction.[16] The physical optics (PO) method is established to construct the RCS of helicopters.[17] The low-RCS millimeter-wave antenna array is designed to reduce reflections of incident waves toward the instrument panel.[18] Unmanned gliders can utilize tilted tail fins to reduce their RCS characteristics.[19] The RCS of the scattering source array is often analyzed using the array synthesis formula and numerical simulation.[20] The formation of drones and gliders can serve as a convenient tool for professional data collection.[21] The PO method has been adopted to optimize the RCS of a 3D glider model.[22] A polarization-conversion metasurface is composed of double-headed arrow unit cells to generate destructive interference and reduce RCS.[23] Image coloring methods have been established to improve the presentation quality of satellite remote-sensing grayscale.[24] The electromagnetic scattering characteristics of the fuselage surface under different postures have been analyzed.[25] Doppler wind lidar has the advantages of a large scanning volume and mobility.[26] The insect average RCS model needs to address issues with morphological and observational parameters.[27] While collecting ground data, the glider can also serve as an observation target for high-altitude platforms. Therefore, remote-sensing observation of gliders and their formations has become a continuous challenge.

As mentioned earlier, this paper proposes a comprehensive method for analyzing the RCS and remote-sensing characteristics of a glider. Surface electromagnetic scattering analysis is beneficial for evaluating the differentiable feature of some connecting parts and preliminarily determining the remote-sensing direction angle. On this basis, the remote-sensing grayscale of multiple gliders or glider formations needs to be reflected. This study has academic value for the stealth design and remote-sensing analysis of gliders.

2. Preliminary configuration

The initial configuration of the glider is shown in Figure 1, where the fuselage adopted a streamlined combination design, the wings featured a positive dihedral angle (A_d) and wingtip configuration, and the tail presented a V-shaped inclination. W_g, L_g, and H_g represent the width, length, and height of the glider, respectively. W_{vt} denotes the horizontal width of the tail fins.

The basic dimensional data can be written in the form of an array:

$$\boldsymbol{P}_g = \begin{bmatrix} L_g & W_g & H_g \end{bmatrix}^T \quad (1)$$

where $\boldsymbol{P}_g$ is the size parameter matrix of the glider. There are significant differences in the operation mode between the V-shaped tail and the vertical tail, where the vertical tail is an independent combination of vertical stabilizer and rudder. The V-shaped tail is a multifunctional integrated design that generates asymmetric aerodynamic forces when two wing surfaces are differentially deflected, achieving rudder-like yaw control. When two wing surfaces are deflected in the same direction, they generate elevator-like torque, achieving pitch control. The relevant geometric dimension data are shown in Table 1.

Table 1. Main size distribution of the glider

Parameter	Value
L_g (m)	7.720
W_g (m)	12.820
H_g (m)	1.320
A_d (°)	1.598
W_{vt} (m)	2.000

High-fidelity unstructured grid technology was implemented to handle the model surface of this glider, as shown in Figure 2, where local operations on lines/surfaces are applied to improve mesh quality along edges, ridges, and narrow surfaces. The grid quality of the V-shaped tail and the wingtips was examined in detail. The preprocessing steps based on the finite element method were the foundation for the subsequent electromagnetic scattering calculations. Compared with expensive material methods, numerical methods based on target geometry are relatively flexible and low-cost approaches.[22]

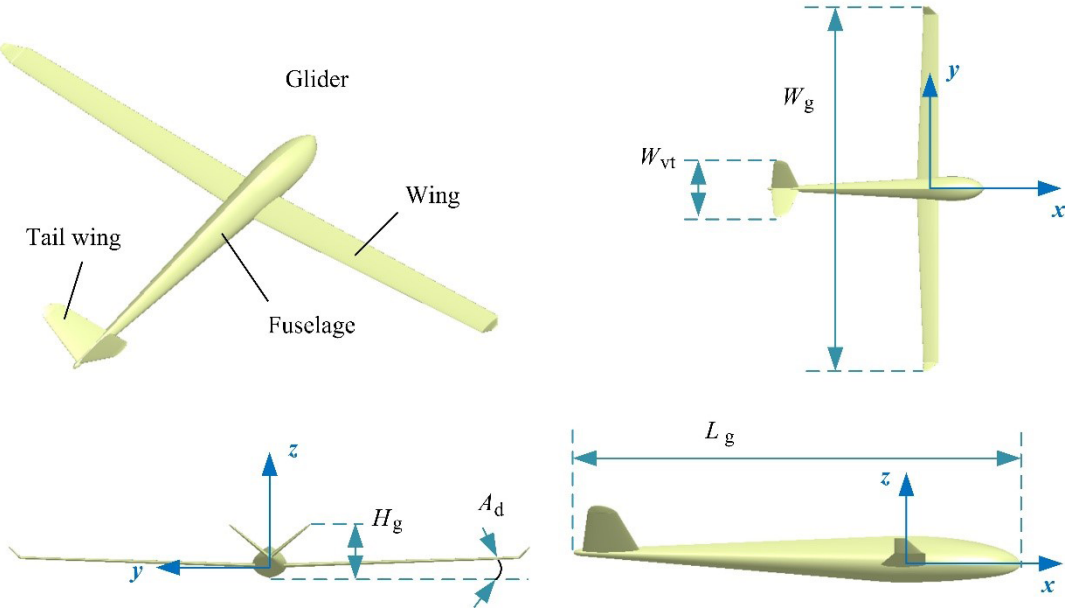

Figure 1. Model establishment of the glider. Image created by the authors with CATIA and Microsoft Visio.

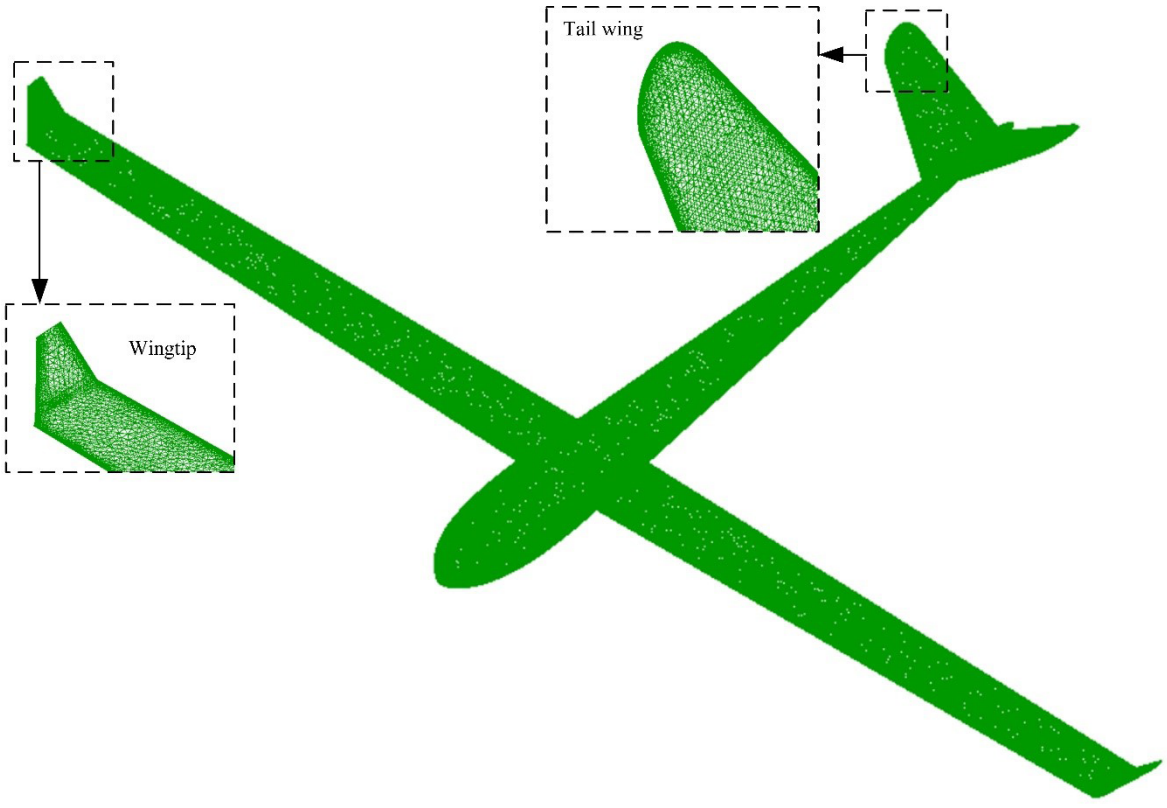

Figure 2. Mesh of the glider model. Image created by the authors with ICEM and Microsoft Visio.

3. Method description

The diagrammatic sketch of the integrated examination method is presented in Figure 3, where x, y, and z represent a coordinate system, with different subscripts corresponding to various platforms. Low-altitude single gliders or multiple gliders can independently participate in remote-sensing imaging of high-altitude airships. Vehicles equipped with radar detectors can move freely on the ground to designated locations to obtain signal characteristics of the glider. For the case of two adjacent gliders, the center position is set as follows:

$$\begin{bmatrix} X_2 \\ Y_2 \\ Z_2 \end{bmatrix} = \boldsymbol{P}_g + \begin{bmatrix} X_1 \\ Y_1 \\ Z_1 \end{bmatrix} + \begin{bmatrix} (2.5+0.2C_s \cdot R_{in}) \cdot L_g \\ (0.5+C_s \cdot R_{in}) \cdot W_g \\ C_s \cdot (R_{in}-0.5) \cdot H_g \end{bmatrix} \left| Z_{20} - Z_1 \right| \le H_{s0} \tag{2}$$

where X, Y, and Z represent coordinates, and a single numerical index is used to distinguish different gliders; Z_{20} represents the original altitude of glider 2; H_{s0} is a pre-set safe height spacing; R_{in} is a random number generated in time; and C_s is the positive or negative sign coefficient:

$$C_s = \begin{cases} 1 & ,\text{if} \quad R_{in} \ge 0.5 \\ -1 & ,\text{else} \end{cases} \tag{3}$$

$$R_{in} = O_{ran}(0, \quad 1) \tag{4}$$

where O_{ran} is a random number generator operator.

In remote-sensing grayscale images, the linear transformation of position needs to maintain the following relationship:

$$(X, \quad Y, \quad \xi) = (x+\Delta X, \quad y+\Delta Y, \quad \xi) \tag{5}$$

where ξ is a grayscale value. As introduced in a previous study[15], the projection difference could be calculated using:

$$\delta_h = -R_P + \sqrt{R_P{}^2 - \Delta h^2 + 2H\Delta h} \tag{6}$$

where δ_h is the projection difference, H is the sensor height, R_P stands for the distance from the sensor to point P, and Δh is the height of point P. For the linear transformation of grayscale:

$$\xi_t = \xi_{t,min} + (\xi_{t,max} - \xi_{t,min}) \frac{\xi_0 - \xi_{0,min}}{\xi_{0,max} - \xi_{0,min}} \tag{7}$$

where subscript *0* refers to the original value, and subscript *t* represents the transformed value. For extremely low raw grayscale, threshold processing is used:

$$\xi_0' = \xi_{th1} \left| \xi_0 - \xi_{th1} \le 0 \right. \tag{8}$$

where ξ_{th1} is the grayscale difference threshold.

In the local coordinate system of the glider, when there is a sideslip on the fuselage:

$$\boldsymbol{M}_g^z(m_g) = \begin{bmatrix} \cos A_s & -\sin A_s & 0 \\ \sin A_s & \cos A_s & 0 \\ 0 & 0 & 1 \end{bmatrix} \times \boldsymbol{M}_g(m_g) \tag{9}$$

where m_g is the glider model, $\boldsymbol{M}_g$ is the grid matrix of the

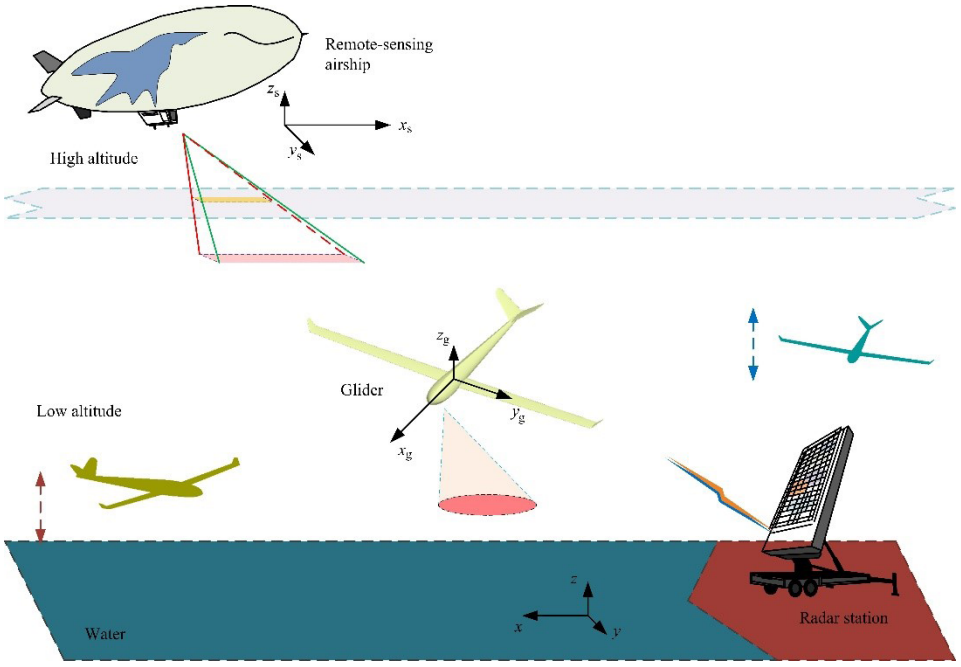

Figure 3. Schematic of the integrated examination method. Image created by the authors with Microsoft Visio and CATIA.

glider model, and A_s is the angle between the nose pointing and the *xz* plane. More information on dynamic RCS under aircraft attitude changes can be found in the study by Zhou and Huang.[25] The definition of RCS is as follows:

$$\sigma = \lim_{R\to\infty} 4\pi R^2 \frac{\left|\boldsymbol{E}_s\right|^2}{\left|\boldsymbol{E}_i\right|^2} = \lim_{R\to\infty} 4\pi R^2 \frac{\left|\boldsymbol{H}_s\right|^2}{\left|\boldsymbol{H}_i\right|^2} \tag{10}$$

where R is the distance from the target to the radar antenna, $\boldsymbol{E}_s$ is the electric field strength of the target scattered wave at the receiving antenna, $\boldsymbol{H}_s$ is the magnetic field strength of the target-scattered wave at the receiving antenna, $\boldsymbol{H}_i$ is the magnetic field strength of the incident wave at the target, and $\boldsymbol{E}_i$ is the electric field strength of the incident wave at the target. PO is used to calculate the RCS of the facet. In the process of using the induction-field approximation to solve the scattering field, the far-field approximation and tangent plane approximation are used. According to the assumption of the PO method:

$$\boldsymbol{J}_s = \begin{cases} 2\boldsymbol{n}\times\boldsymbol{H} & ,Z_{\text{illu}} \\ 0 & ,Z_{\text{dark}} \end{cases} \tag{11}$$

where $\boldsymbol{n}$ represents the unit normal vector of the outer normal direction of $\boldsymbol{r}'$ at the surface of the scatterer, $\boldsymbol{J}_s$ is the surface current, Z_{illu} is the illuminated area, and Z_{dark} is the dark area. For the cross-section of the fuselage with a wedge configuration, as shown in Figure A1, when the top of the fuselage is illuminated, the illuminated area can be represented as:

$$Z_{\text{illu}} = Z_{\text{illu1}} + Z_{\text{illu2}}, \quad \text{when} \quad \frac{\pi}{2} > A_{\text{in}} > \frac{\pi - A_{\text{w}}}{2} > 0 \tag{12}$$

where A_{w} is the angle of the wedge, and A_{in} is the incident angle in the diagram. When the incident angle decreases to a certain extent, the original Z_{llu1} (can be represented as Z_{llu1}') becomes a dark area:

$$Z_{\text{dark}} = Z_{\text{dark1}} + Z_{\text{dark2}}, \quad Z_{\text{dark1}} = Z_{\text{illu1}}', \quad \text{when} \quad 0 < A_{\text{in}} < \frac{\pi - A_{\text{w}}}{2} < \frac{\pi}{2} \tag{13}$$

More relevant descriptions regarding RCS calculations can be found in previous studies.[15,25] The physical theory of diffraction is adopted to determine the RCS contribution of the edge. The RCS of this glider can then be calculated as follows:

$$\sigma = \left| \sum_{i=1}^{N_{\text{F}}} \left(\sqrt{\sigma_{\text{F}}}\right)_i + \sum_{j=1}^{N_{\text{E}}} \left(\sqrt{\sigma_{\text{E}}}\right)_j \right|^2 \tag{14}$$

where σ is RCS, subscript F represents the facet contribution, subscript E represents the edge contribution, N_{E} is the number of edges, and N_{F} is the number of facets. Considering the large range of RCS variation, the logarithmic form is usually used for ease of expression:

$$\sigma\left(\text{dBm}^2\right) = 10\cdot\lg\left[\sigma'\left(\text{m}^2\right)\right] \tag{15}$$

In remote-sensing grayscale images, formations composed of multiple gliders are distributed in a linear or other specific pattern. A backward-expanding sine waveform formation is calculated as follows:

$$X_{i+1} = X_i + \left(3.6 + C_{\text{s}}\cdot R_{\text{in}}\right)\cdot L_{\text{g}}, \quad i = 1,2,3,\ldots,N_g - 1 \tag{16}$$

$$Y_i = \frac{W_{\text{g}}}{10L_{\text{g}}} X_i \cdot \sin\left(\frac{\delta}{4} C_{\text{f}}\cdot X_i\right), \quad i = 1,2,3,\ldots,N_g \tag{17}$$

$$Z_{i+1} = Z_i + \left(2.5 + C_{\text{s}}\cdot R_{\text{in}}\right)\cdot H_{\text{g}}, \quad i = 1,2,3,\ldots,N_g \tag{18}$$

where N_{g} is the number of gliders, and C_{f} is a coefficient. The *x*-axis coordinate of the first glider can be customized.

The validation of remote-sensing imaging methods is shown in Figure 4, and the comparison example is the aircraft in Figure 22 in the study by Zhou.[15] In Figure 4, F_{r} is the radar wave frequency, subscript h represents horizontal polarization, α is the azimuth angle, and β is the elevation angle. The incident wave and observation angle remained unchanged, and the glider appeared at x = −25.16 m with a bright wing surface. The grayscale range of the fuselage and wing surfaces was similar to that of the comparison model. The grayscale distribution of the wingtips, front fuselage, bottom fuselage, and various parts of the wings was reasonable. These results indicate that the remote-sensing modeling method for the glider is effective.

The validation of RCS calculation results is shown in Figure 5, where the comparisons were based on the PO and method-of-moments methods, as in previous studies.[15,25] Within the given azimuth range, the red curve exhibited strong fluctuations with three large peaks, with a mean RCS of 0.7738 dBm^2. When α = 93.25°, the RCS peak was 25.3 dBm^2. Due to the strong mirror scattering effect on the side of the fuselage, the RCS at α = 90.5° exceeded 10 dBm^2. It can be observed that the two curves were similar in shape, peak value, peak position, and mean, with the average RCS of the green curve being 0.7934 dBm^2. As presented in a previous study[22], PO was used to optimize the RCS of the glider; therefore, the RCS algorithm proposed in this paper achieved higher accuracy for slender wings, accounting for edge diffraction. These results indicate that the RCS calculation method is accurate.

4. Results and discussion

4.1. Individual glider

The surface-scattering features of the glider are presented in Figure 6, where the nose of the aircraft exhibited the highest scattering intensity (indicated by deep red).

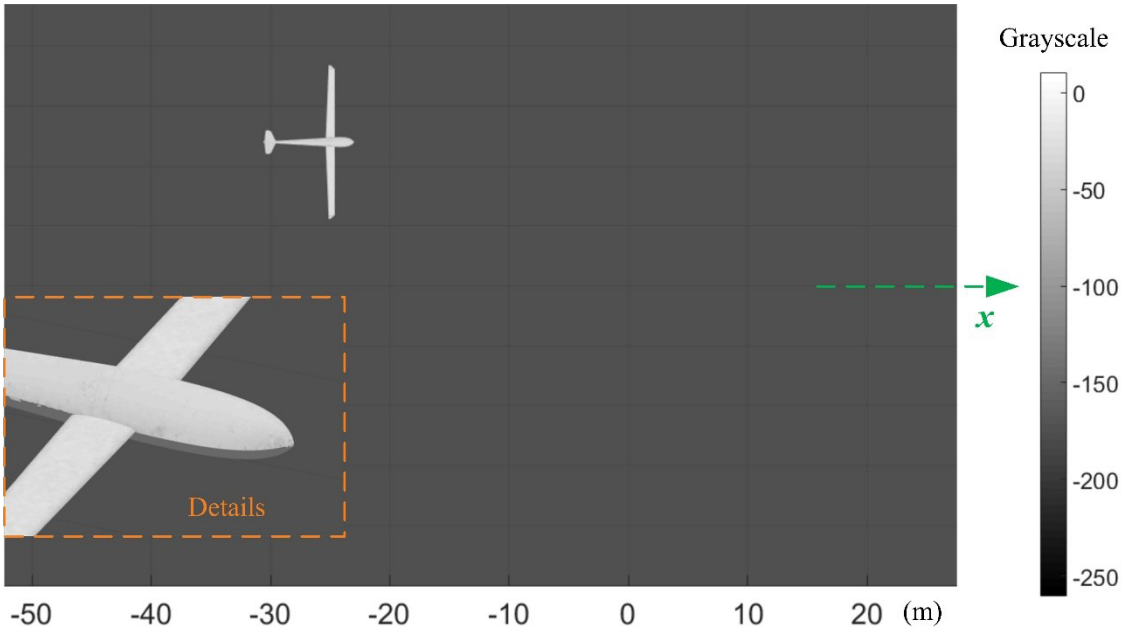

Figure 4. Remote-sensing grayscale verification on the glider: F_{rh} = 7 GHz, α = 279°, and β = 83°. Image created by the authors with Matlab and Microsoft Visio.

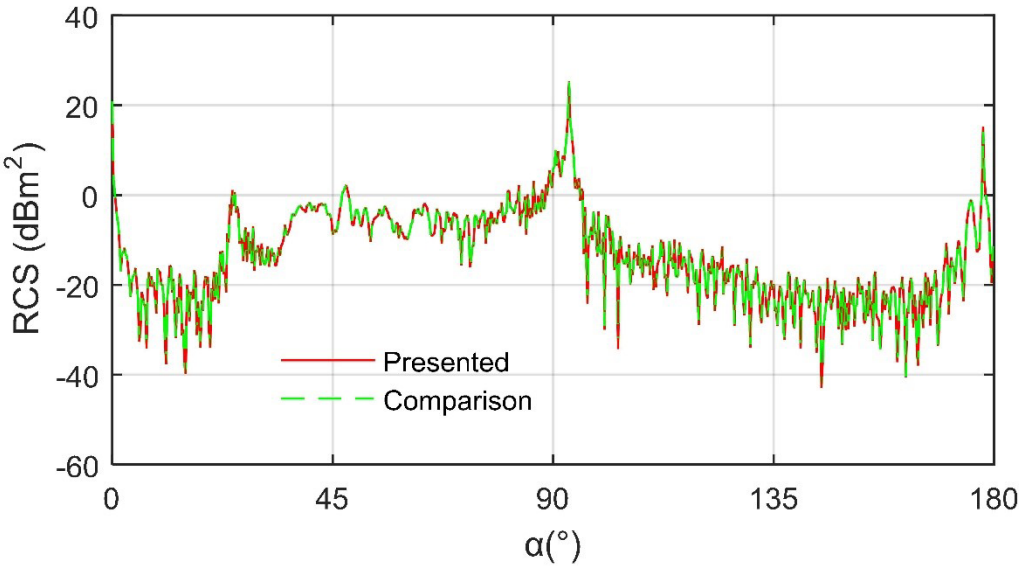

Figure 5. Radar cross-section calculation verification on the glider: F_{rh} = 6 GHz, β = 2°, and A_s = 0°

Because of the use of elliptical curves as the horizontal contour and conventional spline curves as the cross-sectional configuration of the front fuselage, the generated surface of the nose could not effectively deflect the incident wave to a non-threatening direction. The front half of the upper surface of the wing is characterized by red, orange (approximately −62), and a small amount of yellow (about −80). Due to the obstruction of the curved surface near the raised ridge line on the back of the fuselage, the other side of the fuselage is a blue (close to −155) feature. Under the current incident conditions, the upper surfaces of the two tail fins exhibited a strong contrast in scattering intensity: one with a large orange area, and the other with a large blue area. These results indicate that the established method is feasible for analyzing the electromagnetic scattering features of the glider surfaces.

The RCS curves of the glider at different elevation angles are shown in Figure 7, with a mean RCS for the β = 3° line of 0.8266 dBm^2 (Table 2). The maximum RCSs across the four curves were close, with the highest RCS peak on the β = 5° line, at α = 93.25°, being 24.4146 dBm^2. The azimuth angles corresponding to the maximum peak on the four curves were almost the same because, at this time, the side of the fuselage, the trailing edge of the wing, and the tail provide scattering contributions, with the azimuth angle at which the maximum appears on the β = 10° curve being 93°. The relationship between radar detection distance and target RCS can be quantified by the radar equation: detection distance is proportional to the fourth root of the target RCS. There was a significant shift in the local peak positions of the four curves within the azimuth range of 15–29.5°, with the RCS on the β = 7° line at α = 21° being −0.2983 dBm^2. Within the azimuth range of head and tail direction, the RCS curve of the glider exhibited a large peak value, exceeding 15 dBm^2. These results indicate that, under the given conditions, the mean RCS index of the glider increases slowly with increasing elevation angle.

Table 2. Radar cross-section (RCS) curve of the glider (A_s = 0°, α = 0–180°, and F_{rh} = 6 GHz)

β (°)	RCS mean (dBm^2)	RCS peak (dBm^2)
3	0.8266	25.0604
5	1.1469	24.4146
7	1.2573	24.5831
10	1.6115	25.3957

The RCS comparison of the glider at different radar frequencies is shown in Figure 8, where the average RCS for the F_{rh} = 5 GHz curve was 0.5396 dBm^2. At α = 93.25°, the green curve reached its maximum peak of 25.1607 dBm^2, while the maximum of the F_{rh} = 7 GHz curve was 25.2356 dBm^2. Within the azimuth range of 33.5–36.25°, the red curve was significantly lower than the other two. The radar equation states that as the RCS of the target increases, the radar detection range increases significantly. Due to the scattering contribution of the curved surface near the trailing edge of the wing and the tail of the fuselage, a large peak appeared at α = 177.75°. Within the azimuth range of 99.25–169.5°, all three curves exhibited severe fluctuations, with the red line showing the smallest minimum. The mean RCS for the F_{rh} = 7 GHz curve was 0.3759 dBm^2, with the minimum being −54.9 dBm^2 at α = 134.5°. When α = 24.25°, the three curves exhibited a small peak. Compared with the PO method presented in a previous study[22], the RCS calculation here also accounted for diffraction from the front and rear edges of the wing, the tail edge, and the fuselage edge. Compared with the aircraft in a previous study[15], the glider equipped with a V-shaped tail in this paper exhibited lower RCS in the lateral azimuth angle.

4.2. Integrated analysis

The remote-sensing imaging of three gliders (GL1, GL2, and GL3) is shown in Figure 9, where GL1 appeared at x = 62.13 m. The heads of the three gliders are clearly presented in light gray (around −15). At y = 25.10 m, the angle between the glider's nose pointing and the positive x-axis was 15°, with the upper surface of the tail beam of the rear fuselage (GL3) being gray (near −38). At y = 6.607 m, the angle between the symmetrical plane of GL1 body and the x-axis was 27°, and the fuselage, wings, and tail could be clearly distinguished. When x = −18.71 m, the nose of GL2 was pointing at an angle of 50° to the positive x-axis and pointing toward the negative y-axis, with obvious dark gray (about −160) features on the side of the fuselage and one tail wing and a dark gray area on a wing tip. These results indicate that the established remote-sensing imaging method is effective for analyzing the grayscale features of multiple gliders. Compared with previous results[15], the integrated examination method here accounts for aircraft orientation and multi-aircraft mode. To ensure grayscale details, it is recommended to set the minimum local magnification to 2 and the display resolution to 1200 × 1200. A denoising and coloring method based on satellite remote-sensing grayscale images was presented in a previous study[24], providing a development direction for the grayscale transformation in this paper.

The surface-scattering features of the glider are provided in Figure 10, where the darkest red color (close to −25) was visible on the surface of the nose and the leading edge of the wings. Because of the influence of the azimuth angle and a small amount of sideslip on the fuselage, the orange color of one tail wing was significantly darker than

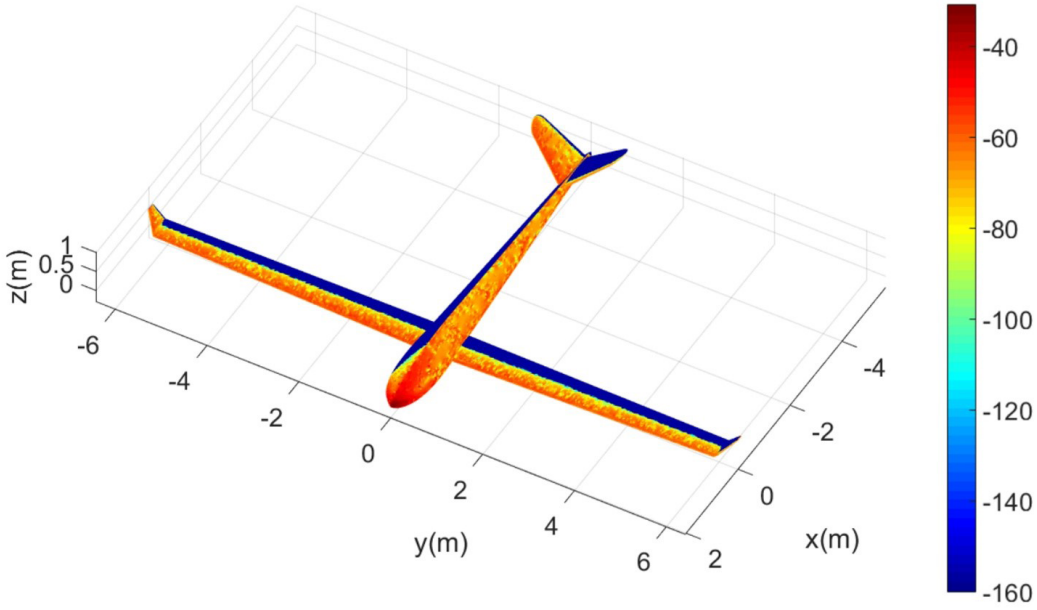

Figure 6. Surface-scattering characteristics of the glider: F_r = 8 GHz, β = 1°, A_s = 0°, and α = 12°
Note: Radar cross-section unit: dBm².

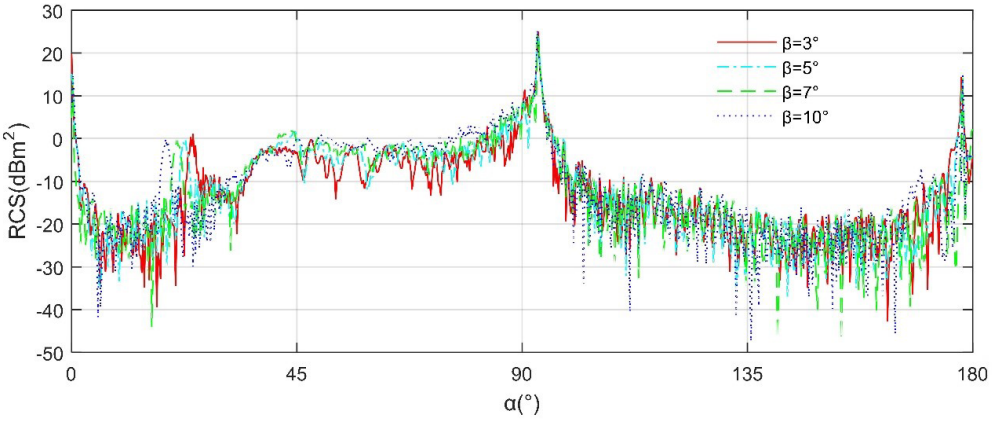

Figure 7. Radar cross-section (RCS) curve of the glider: A_s = 0° and F_{rh} = 6 GHz

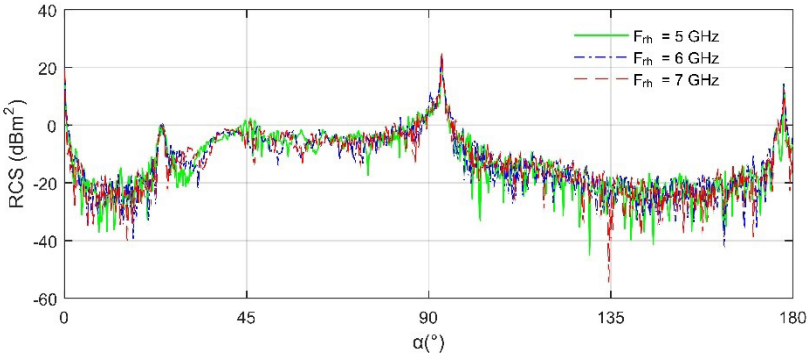

Figure 8. Radar cross-section (RCS) results of the glider: A_s = 0° and β = 3°

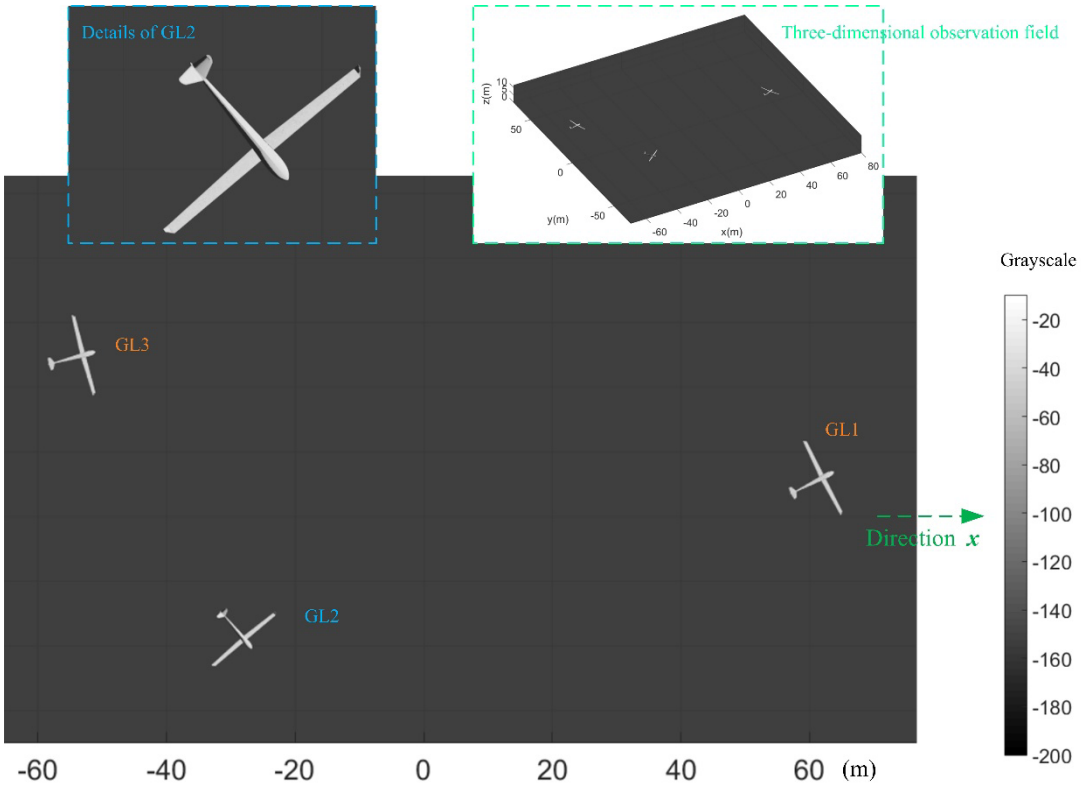

Figure 9. Remote-sensing grayscale image of three gliders (GL1, GL2, and GL3): F_r = 6 GHz, α = 18°, and β = 37°

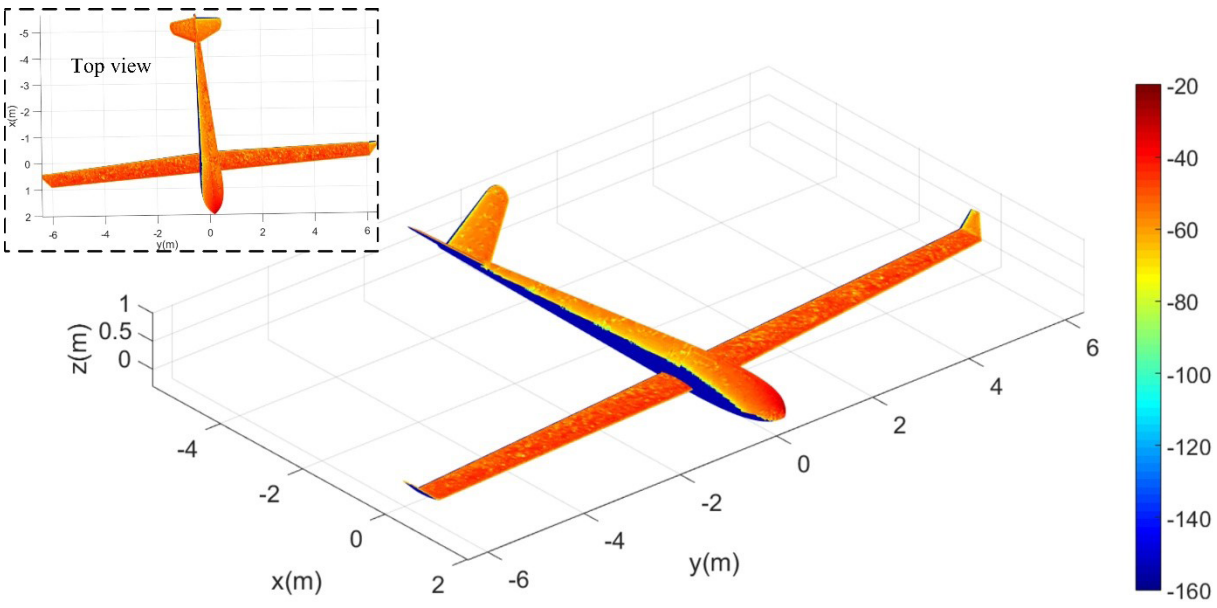

Figure 10. Surface-scattering characteristics of the glider: F_r = 7 GHz, β = 25°, A_s = 5°, and α = 22°
Note: Radar cross-section unit: dBm^2.

that of the other tail wing. The illuminated area of the wing was almost dark red and red, with a small amount of orange (approximately −65) and yellow (around −72). Surface materials have a significant impact on RCS, mainly by regulating the reflection, absorption, and scattering of radar waves through their electromagnetic properties (such as dielectric constant, magnetic permeability, and conductivity) and surface structure (such as roughness). Due to the obstruction at the top of the fuselage, blue and a small amount of yellow appeared on one side of the body. The upper surface of a wingtip was orange and yellow, and the tail of the wingtip was blue. Analyzing the surface electromagnetic scattering of a single glider is beneficial for understanding its remote-sensing grayscale distribution. The surface electromagnetic scattering characteristics of a tandem helicopter were analyzed in a previous study[25], providing a reference for subsequent research on gliders with powered propellers.

The grayscale features of multiple gliders (GL1–GL6) are presented in Figure 11, where GL1–GL5 formed an approximately linear formation. At x = 75.76 m (GL6), one tail wing of GL6 displayed a brighter light gray colour (approximately −25) than the other (close to −42). The grayscale features of the fuselage, wings, and wingtips could be distinguished; the angle between the symmetrical plane of the fuselage and the x-axis was 29°; and the grayscale difference on both sides of the top ridge line of the fuselage persisted after local magnification. At x = 23.32 m (GL5), a narrow dark gray (near −162) feature appeared on the side (y = 16.86 m) of the fuselage through local observation. The remaining gliders in this linear queue appeared near y = 31.02 m. At x = 110.7 m (GL2), the wings and fuselage appeared light gray, and one wing tip showed a deeper gray colour than the other. The influence of surface materials on remote-sensing imaging mainly manifests through the reflection, absorption, and emission characteristics of electromagnetic waves, which determine the signal strength and quality received by the sensor and thereby directly affect the accuracy and interpretability of the imaging. These results suggest that the established remote-sensing imaging method is effective for analyzing the grayscale characteristics of glider formations. Compared with a previous study[15], the remote-sensing grayscale characteristics of diverse formations are presented in this study. Doppler lidar is an emerging active remote-sensing instrument with great potential to improve numerical models.[26] The radar monitoring technology for large-scale insects has practical value[27], providing a reference for continued research on a large number of gliders.

4.3. Backward diffusion formation

The remote-sensing image of the glider formation is provided in Figure 12, where the blue dashed line is the projection line of the backward diffusion formation. At x = 38.12 m, GL11 appeared alone outside the formation, and its grayscale features of the fuselage, wings, and tail could be clearly identified. The angle between the nose pointing and the positive x-axis was 120°. The center of GL10 in the formation was located at x = −270 m and y = 31.39 m, with a narrow dark gray stripe (approximately −158) appearing at the connection (y = 30.95 m) between the fuselage and the wings. Because of the dihedral angle design of the wing, the gray color (near −22) on one wing of GL6 at x = −175.6 m was lighter than the other wing (grayscale close to −35) under current conditions. At x = −135.2 m, there was a significant difference in the grayscale features on both sides of the top ridge line of the fuselage, which can be observed through local magnification. Taking

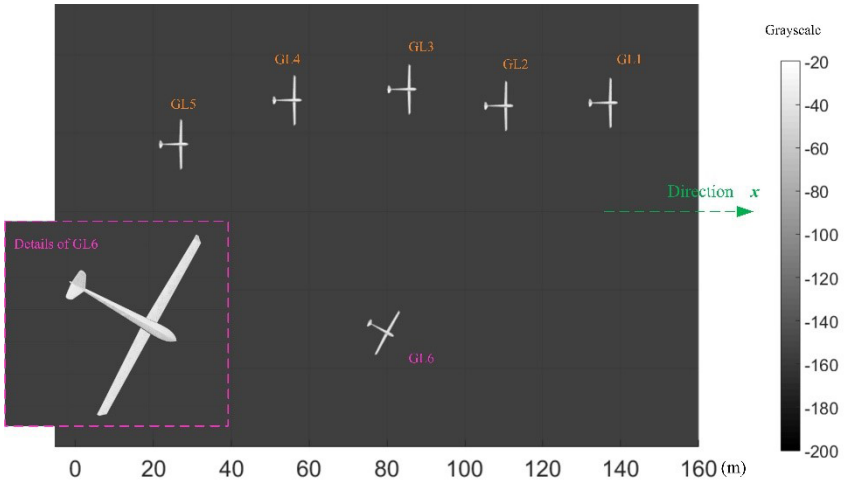

Figure 11. Remote-sensing grayscale image of multiple gliders (GL1–GL6): F_r = 8 GHz, β = 51°, and α = 110°

the coordinates of the center point of the glider's local coordinate system in the grayscale image as an example, the coefficient of determination index for curve fitting was 1, where C_f = 1/10. Remote-sensing data with highly rough ocean surfaces can provide certain support for scene background selection.[28] These results reveal that the established imaging method and transformation operation are feasible for learning the grayscale characteristics of complex formations composed of gliders.

The grayscale characteristics of a complex formation consisting of 16 gliders are shown in Figure 13, where a single glider appeared at the front of the queue at x = 15.1 m. At the current observation scale, the grayscale visual effect of the rear fuselage tail beam (as seen at x = −391.5 m) was significantly reduced, indicating that a larger display interface can achieve better rendering. The last glider in the queue appeared at x = −442.3 m, while the first glider in the formation appeared at x =−20.79 m. For the case (x = 15.1 m and y = −33.53 m) outside the formation, the angle between the symmetry plane of the fuselage and the x-axis was 25°. Because of the adoption of regular queue flight, this glider formation could be distinguished in the grayscale image, which is also one of the indicators for distinguishing individual free-flying aircraft. At x = −108.6 m, the head, middle of the fuselage, and wings of the glider still displayed a light gray color (approximately −25), and the two tail fins showed a slightly stronger visual effect than the end of the tail beam.

Overall, gliders in a backward-spreading formation may appear visually complex and disorganized in grayscale

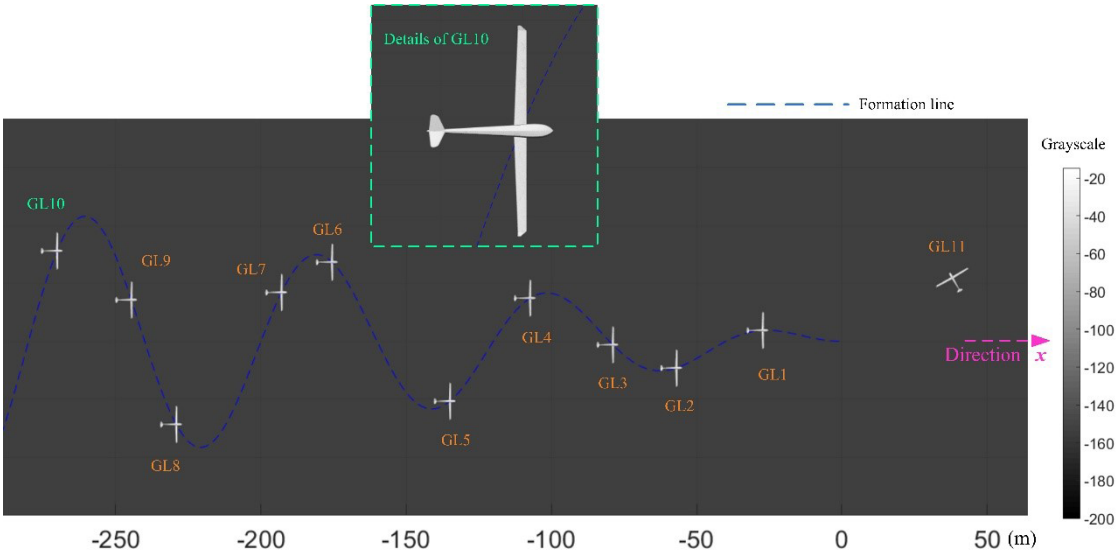

Figure 12. Remote-sensing grayscale image of the glider formation (GL1–GL11): F_r = 8 GHz, β = 51°, α = 110°, and N_g = 10

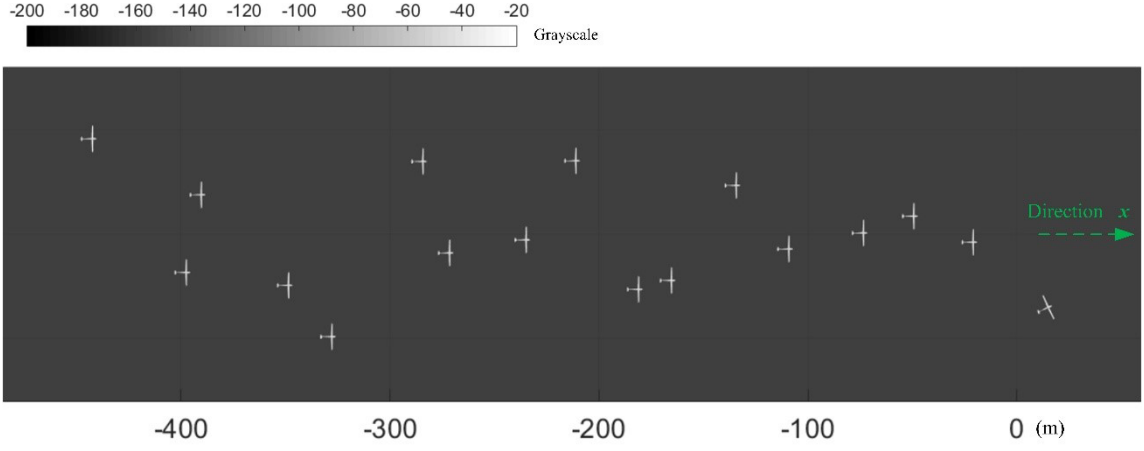

Figure 13. Remote-sensing grayscale image of the glider formation: F_r = 9 GHz, β = 68°, α = 129°, and N_g = 16

vision, while there is a mathematically predictable sinusoidal pattern to follow: the planar layout of this formation is represented by a sinusoidal curve that diverges backward. In addition, a formation composed of multiple gliders has a relatively uniform flight direction under normal circumstances and produces more radar signal features.

5. Conclusion

Based on the preliminary design glider model, an integrated examination method that considers electromagnetic scattering calculations and remote-sensing imaging has been established. The RCS and remote-sensing grayscale images of the glider were analyzed. The following conclusions can be drawn from this article:

(i) Under specific observation conditions, analyzing the large differences in electromagnetic scattering characteristics between the tail wings or the sides of the fuselage is beneficial for understanding the dark gray areas that appear in remote-sensing grayscale. As the elevation angle increases within the given range, the average RCS of the glider increases by 0.7849 dBm^2, the peak RCS first decreases and then increases, and the peak position remains almost unchanged.

(ii) Due to the wedge design on the top of the fuselage, the intuitive effect of the fuselage in remote-sensing grayscale images presents a contrast between light gray and gray (even dark gray), and the dark gray part of the tail wing is visually blended with the dark background colour. The body provides a significant scattering contribution for peak values exceeding 25.1 dBm^2, and can also form a relatively stable visual effect in grayscale images.

(iii) In remote-sensing grayscale images, the nose pointing of a single glider can be distinguished, and a linear formation composed of multiple gliders is easy to observe. The visual effect of a backward-spreading formation appears chaotic, but it actually follows certain patterns. For complex formations, local magnification or large display interfaces can yield better graphical rendering.

In future research, multi-band imaging and target recognition using artificial intelligence for gliders are directions worth exploring.

Acknowledgments

None.

Funding

This research was funded by the China Postdoctoral Science Foundation (Grant No.: BX20200035, 2020M680005).

Conflict of interest

The authors declare they have no competing interests.

Author contributions

Conceptualization: All authors
Formal analysis: All authors
Investigation: All authors
Methodology: Zeyang Zhou
Visualization: Zeyang Zhou
Writing–original draft: Zeyang Zhou
Writing–review & editing: All authors

Ethics approval and consent to participate

Not applicable.

Consent for publication

Not applicable.

Availability of data

The original contributions presented in the study are included in the article, and further inquiries can be directed to the corresponding author.

References

1. Haghighi AN, Nolin RD, Pundsack G, Craine N, Stratsilatau A, Bailey SCC. High-altitude balloon-launched uncrewed aircraft system measurements of atmospheric turbulence and qualitative comparison with infrasound microphone response. *Atmos Meas Tech*. 2024;17:4863–4889.

   doi: 10.5194/amt-17-4863-2024

2. Mathews AJ, Singh KK, Cummings AR, Rogers SR. Fundamental practices for drone remote sensing research across disciplines. *Drone Syst Appl*. 2023;11:1-22.

   doi: 10.1139/dsa-2023-0021

3. Ye SB, Xiong JJ. Dynamic RCS behavior of helicopter rotating blades. *Acta Aeronaut Et Astronaut Sin*. 2006;27(5):816-822.

4. Qu Z, Li C, Hao Y, Yan F, Yang Y. Project of high altitude balloon launched micro glider: Aircraft design, control and flight test. *Int J Micro Air Veh*. 2020;12:1-20.

   doi: 10.1177/1756829320979955

5. Chang M, Zhou Z, Wang R. Primary parameters determination for year-round solar powered aircraft of wing-sail type at higher latitudes. *Acta Aeronaut Sin*. 2014;35(6):1592-1603.

6. Cunico MWM, Cavalheiro JDM. Experimental and

numerical analysis of 3D-printed objects based on oriented anisotropic cells. *Design+*. 2025;2(1):3779.

doi: 10.36922/dp.3779

7. Hou XG, Huang J. Study of model build of double-podded joined-wing solar powered aircraft. *Aircr Des*. 2013; 33(1): 6-9. [in Chinese]

doi: 10.19555/j.cnki.1673-4599.2013.01.002

8. Abbe G, Smith H. Technological development trends in Solar-powered Aircraft Systems. *Renew Sustain Energy Rev*. 2016;60:770-783.

doi: 10.1016/j.rser.2016.01.053

9. Ma DL, Bao WZ, Qiao YH. Study of flight path for solar-powered aircraft based on gravity energy reservation. *Acta Aeronaut Sin*. 2014;35(2):408-416.

10. Bolohin A, Bolohina Y, Tymchuk Y. Ranking of the technical condition of aircraft according to the diagnostic data of the glider design. *Syst Res Inf Technol*. 2025;2:98–105.

doi: 10.20535/SRIT.2308-8893.2025.2.06

11. Zhang LG, Zhang J. Key technology and development of solar aircraft. *Mech Eng*. 2018;4:1-4+7. [in Chinese]

12. Marques HG, Agarwal RK. A methodology for predicting solar power incidence on airfoils and their optimization for solar-powered airplanes. *Proc Inst Mech Eng Part G J Aerosp Eng*. 2015;229(7):1267-1279.

doi: 10.1177/0954410014549391

13. Klesh AT, Kabamba PT. Solar-powered aircraft: Energy-optimal path planning and perpetual endurance. *J Guid Control Dyn*. 2009;32(4):1320-1329.

doi: 10.2514/1.40139

14. Yan JL, Hu ZF. A Design of Fixed-wing Aircraft with Solar Energy Power Source. *Mod Inf Technol*. 2019;3(3):160-163+167. [in Chinese]

15. Zhou Z. Comprehensive Discussion on Remote Sensing Modeling and Dynamic Electromagnetic Scattering for Aircraft with Speed Brake Deflection. *Remote Sens*. 2025;17(10):1706.

doi: 10.3390/rs17101706

16. Modi AY, Balanis CA, Birtcher CR, *et al*. Novel design of ultrabroadband radar cross-section reduction surfaces using artificial magnetic conductors. *IEEE Trans Antennas Propag*. 2017;65(10):5406-5417.

doi: 10.1109/TAP.2017.2734069

17. Bao X, Zhang Y, Liu K. Calculation and analysis on radar scattering characteristics of two types of utility helicopter. *Helicopter Tech*. 2012;3:11-14+33. [in Chinese]

18. Vasanelli C, Bögelsack F, Waldschmidt C. Reducing the radar cross section of microstrip arrays using AMC structures for the vehicle integration of automotive radars. *IEEE Trans Antennas Propag*. 2018;66(3):1456-1464.

doi: 10.1109/TAP.2018.2794410

19. Yin P, Jia GW, Yang XX. Wai jun wu ren ji yin shen she ji fa zhan yan jiu [Research on the development of foreign military UAV stealth design]. *Aerodyn Missile J*. 2021;12:69–74.

doi: 10.16338/j.issn.1009-1319.20210192

20. Guo J, Yin HC, Ye SJ, *et al*. Novel technology for electromagnetic characteristic simulation of helicopter blades. *Acta Aeronaut Et Astronaut Sin*. 2019;40(7):322732.

21. Asadzadeh S, de Oliveira WJ, de Souza Filho CR. UAV-based remote sensing for the petroleum industry and environmental monitoring: State-of-the-art and perspectives. *J Pet Sci Eng*. 2022;208:109633.

doi: 10.1016/j.petrol.2021.109633

22. Fang R, Wu YM, Ye H. End-to-end Differentiable RCS Optimization on 3D Geometry Based on Physical Optics Method. *IEEE J Multiscale Multiphysics Comput Tech*. 2025;10:246-258.

doi: 10.1109/JMMCT.2025.3569766

23. Ameri E, Esmaeli S H, Sedighy S H. Ultra wideband radar cross section reduction by using polarization conversion metasurfaces. *Sci Rep*. 2019;9(1):1-8.

doi: 10.1038/s41598-018-36542-6

24. Fu Q, Xia S, Kang Y, Sun M, Tan K. Satellite Remote Sensing Grayscale Image Colorization Based on Denoising Generative Adversarial Network. *Remote Sens*. 2024;16(19):3644.

doi: 10.3390/rs16193644

25. Zhou Z, Huang J. X-Band Radar Cross-Section of Tandem Helicopter Based on Dynamic Analysis Approach. *Sensors*. 2021;21(1):271.

doi: 10.3390/s21010271

26. Liu Z, Barlow JF, Chan P-W, *et al*. A Review of Progress and Applications of Pulsed Doppler Wind LiDARs. *Remote Sens*. 2019;11(21):2522.

doi: 10.3390/rs11212522

27. Wang R, Kou X, Cui K, *et al*. Insect-Equivalent Radar Cross-Section Model Based on Field Experimental Results of Body Length and Orientation Extraction. *Remote Sens*. 2022;14(3):508.

doi: 10.3390/rs14030508

28. Torabi M, Shahidi R, Gill EW. Single-Scattering Radar Cross Section of the Ocean Surface Without the Small-Slope and Height Assumptions. *Radio Sci*. 2025;60,e2025RS008265.

doi: 10.1029/2025RS008265

Appendix

Compared with the conventional curved cross-section of the fuselage, the sharp split configuration is advantageous for deflecting specific incident waves, as shown in Figure A1. Due to the presence of sharp edges, edge diffraction must also be considered.

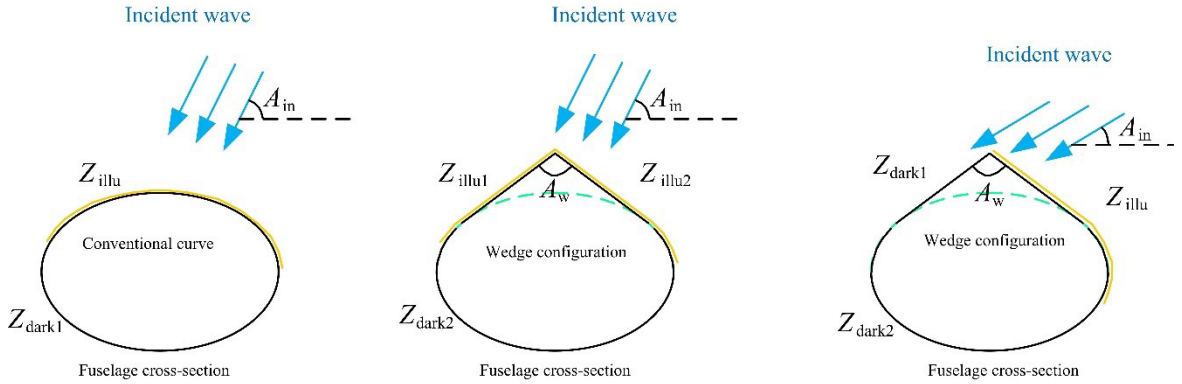

Figure A1. Schematic of scattering analysis of the wedge configuration of the fuselage cross-section